von Karman Institute for Fluid Dynamics

Lecture Series 2025-01

MEASUREMENT, MODELLING AND SIMULATIONS TECHNIQUES FOR NOVEL AIRCRAFT ARCHITECTURES

November 4-6, 2024

AEROACOUSTIC INSTALLATION EFFECTS IN PROPULSION SYSTEMS

M. Roger
Ecole Centrale de Lyon, France

1 Introduction

The design of a propeller or rotor is initially aimed at producing thrust or lift, which is a matter of steady-state aerodynamics of blades, irrespective of zero-average variations due to the presence of neighboring surfaces or of non-homogeneities in the flow. The propeller is said isolated and placed in ideal aerodynamic conditions. Such conditions include hover or zero advance-ratio, for rotors and propellers, respectively, and vertical or horizontal advancing motion, parallel to the axis. They are associated with steady-loading noise and thickness noise, as stated by Ffowcs Williams & Hawkings' analogy[1].

Any deviation from the aforementioned ideal situations generates additional time variations of the flow relative to the blades, entering the scope of unsteady aerodynamics. As a consequence, it also generates additional loading noise. Rigorously, two causes of unsteady aerodynamics should be distinguished, namely the ingestion of flow distortions due to operation, environmental conditions and maneuvers, on the one hand, and flow distortions due to the presence of surrounding surfaces, such as wing, struts, fuselage and so on, as well as the ground, on the other hand. Other aspects associated with the combination of multiple rotors in distributed electric propulsion systems (DEP) belong the same category. For simplicity, all will be considered in the same way, as responsible for what is referred to as the aerodynamic installation effects. These effects are addressed in this lecture from the phenomenological standpoint, mostly referring to experiments or numerical simulations, for illustration. Their low-order modeling in engineering context is the matter of the lecture *Semi-analytical and low-order models applied to isolated and installed propulsors*.

The variety of aerodynamic installation effects is too large for a dedicated lecture to be exhaustive. The present document focuses on representative examples that should be systematically assessed by inspection of each particular case. Besides, let's mention a couple of recent studies as open doors to aspects deserving attention, in particular in drones and eVTOL aircraft architectures. For instance, takeoff/landing phases or operations of tilting rotors are accompanied with off-design oblique flows through rotor discs, sometimes from downstream, as investigated by Hanson et al. (2024). Synchrophasing of propellers in close vicinity to each other induces acoustic interference but also generates specific aerodynamic interactions. This is addressed, for instance, by Pandey et al. (2024). Starting operation of static rotors generates recirculating flows, which need time to establish, progressively causing noise increase as the distortions develop (see Tinney and Valdez (2024)).

Preceding considerations refer to the modification or to the production of new sources of aerodynamic noise on rotating blades, because of practical installation and operation, paying no attention to sound propagation. Now, introducing solid surfaces in the propagation medium also restructures the radiating properties of the sources by a complex diffraction mechanism, with respect to how they would radiate in ideal unbounded medium. This difference between acoustic signatures in free-field and installed configurations is referred to as the acoustic installation effect, understood with unchanged sources. But the joint operation of multiple rotors also produces changes of the acoustic signature, leading to include this in the category of acoustic installation effects. Typically, rotating-

[1] In principle, mean-flow distortions around the blades contribute to quadrupoles; this part is negligible at subsonic Mach numbers.

speed mismatch between multiple propellers or rotors generates beating, or is marked by tone dedoubling in sound spectra, as pointed out by Zhang (2017) and Ahmed et al. (2024). In quadrotors, the mismatch is inherent to different rotational speeds of the front and rear rotors, either for the need to generate advancing flight or because the airframe is not symmetrical. It also results from continuous adjustment performed by the controllers of individual motors, in order to ensure global stability.

In analytical modeling approaches, aerodynamic and acoustic installation effects are treated explicitly and separately, the former being only involved in the definition of the equivalent sound sources of the analogy, and the latter being involved in the radiation from the sources, in other word concentrated in the Green's function used to solve the equation of the analogy. Indeed, analytical models are usually formulated for each previously identified and isolated sound-generation or sound-propagation mechanism. The situation is different in compressible numerical approaches, which potentially reproduce the complete intricate physics as a whole and accurately, provided that they are previously validated and proved sufficiently resolved in terms of mesh refinement and numerical scheme quality. This means that the two aformentioned installation effects can be hard to distinguish. Yet, to summarize and focus the scope of this lecture, acoustic installation effects will mainly refer to the modification of the intrinsic radiating properties of aerodynamic sound sources by airframe and surrounding surfaces (scattering or diffraction), the sources being assumed the same in installed and free-field configurations. The address of aerodynamic installation effects will be reduced to sound sources generated by asymmetric inflow or distortions around solid bodies. Last but not least, the lecture is devoted to the tonal noise, as dominant contribution in drones and eVTOL aircraft.

For a recent review of challenges in DEP, in particular addressing some of the presently discussed installation effects, the reader can also refer to Greenwood et al. (2022).

2 Aerodynamic Installation Effects

2.1 Inflow Distortions

In order to induce periodic blade forces, a distortion must take the form of a non-axisymmetric pattern in the reference frame of the rotor or propeller[2]. A first example is the ground vortex formed as a propeller with horizontal axis is operating in static conditions, before takeoff. This vortex develops around the particular streamline starting from a point on the ground and entering the propeller disc, as discussed by Colehour and Farquhar (1971) (Fig. 1-a). It is most often concentrated, inducing impulse-like variations of angle of attack on the blades. Similarly, as a hovering rotor operates close enough to the ground, the downswash produced by the rotor is accompanied with a strong recirculation, azimuthally non-homogeneous because of the fuselage. In the latter case, the gross features of the distortion are expectedly less concentrated, so that less impulsive unsteady loads are produced. By the way, Fig. 1 is also the occasion of identifying other effects. Firstly, in Fig. 1-a, the air intake of the turboprop located just below the spinner induces a potential distortion of the flow upstream. As the blades cross this local distortion, they experience

[2]Note that radial variations of an axisymmetric mean flow only generate steady-state aerodynamics on the blades.

additional unsteady loads, combining with those from the ground vortex. Secondly, in both subplots (a) and (b), the ground causes a reflection of the direct sound field of the propeller or rotor, which contributes to the acoustic installation effects.

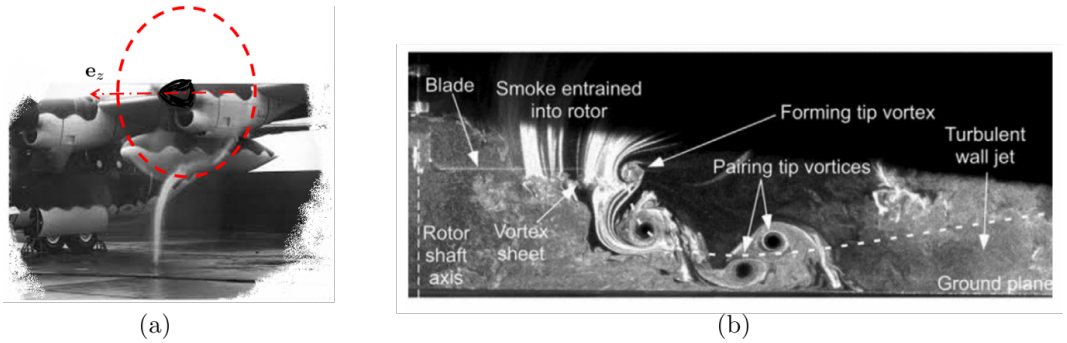


Figure 1: Visualization of typical infow distortions in open rotors. (a): ground vortex (picture from the Internet); (b): ground-induced recirculation, also featuring the formation of tip vortices, from Mehrabi and Davari (2020).

Another typical azimuthal inflow distortion is produced as a rotor is put in forward motion (edgewise flight) with a negative pitch, or nose-down attitude, as in the case of advancing helicopters or quadrotor drones (see Fig. 2). This effect is detailed in section 2.1.1. For a front rotor, the distortion results from the combined avancing and rotating motions. For tandem rotors, the slipstream of the front rotor possibly contributes to the inflow through the rear rotor. This is illustrated in Fig. 2, keeping in mind that a large variety of interaction features can be encountered, depending on relative advancing speed and induced velocity, effect of the airframe, rotor-rotor distance and so on. The tilt-rotor concept and all maneuvers it allows, going from classical hover to advancing CTOL-like flight[3], in the context of eVTOL aircraft (mentioning the V22 and Joby DEP technology as examples), give a crucial importance to these effects.

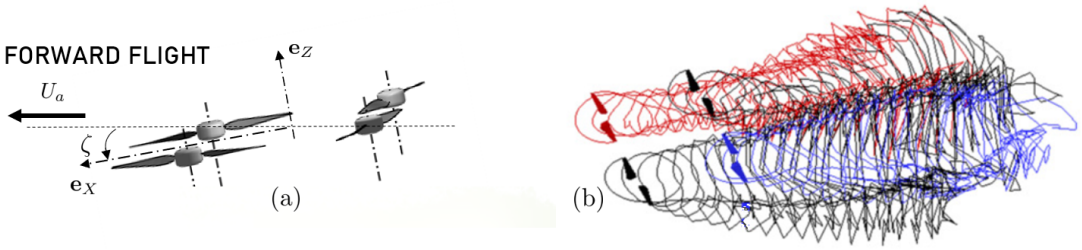


Figure 2: (a): nose-down attitude of a quadrotor for forward flight, generic configuration. (b): simulation of wake interactions for a quadrotor in forward flight, from Ko and Lee (2023).

[3]CTOL: Conventional take-off and landing; (e)VTOL: vertical take-off and landing, 'e' for electric.

2.1.1 Edgewise Flow in Forward Flight and Propeller Incidence

As a hovering rotor is moving horizontally, the advancing speed combines with the tangential motion of any rotating blade segment, resulting in periodic changes of the angle of attack and associated periodic variations of the aerodynamic forces. In practice, for rotorcraft, the advancing motion is obtained by slightly tilting the rotor to adopt a nose-down attitude, so that an oblique mean flow results, relative to the rotor. Forward flight appears as a source of BLH, inherent to the technology. Similar variations are faced as an aircraft propeller is flying at non-zero incidence. In this case, the relative mean flow obliquely enters the propeller disc with a quite small angle with respect to the axis. In the rotorcraft case, the relative mean-flow angle is close to the rotor plane. The common feature of both situations is the nearly sinusoidal variations of angle of attack experienced by blade segments. The induced fluid velocity generated by rotor lift or propeller thrust still increases the complexity of this fundamental oblique-flow effect.

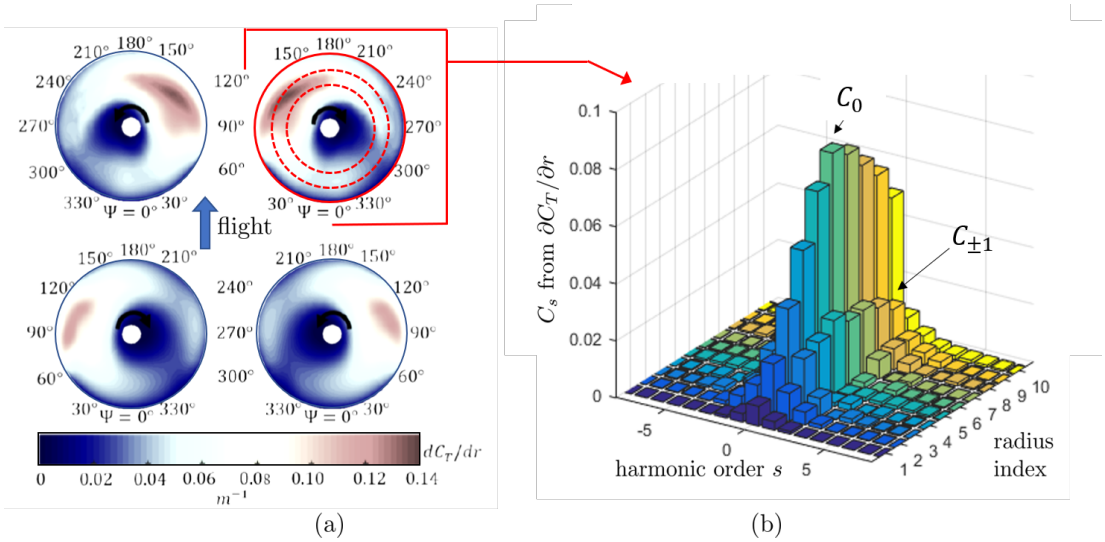


Figure 3: (a): sectional thrust coefficient maps, from simulations by Misiorowski et al. (2019). Focus on the front starboard rotor disc. (b): corresponding loading harmonics for a 10-strip splitting.

As an example, numerical flow simulations reported by Misiorowski et al. (2019) are post-processed here to determine the blade-loading harmonics. The configuration is that of a quadrotor in advancing flight with a negative pitch angle of 5° and flight speed of 10 m/s. The airframe is not considered, so that only the effects of edgewise flow, and to a lower extent of rotor-rotor interactions, are reproduced, with no blockage of induced flows. For each rotor, the simulation gives access to the sectional thrust coefficient, in the form of a map on the rotor disc. The front starboard rotor is selected in this section to illustrate the post-processing, see Fig. 3-a. The disc is split into 10 annular strips from hub to tip (corresponding to 10 elements in the BET, see the lecture *Semi-analytical and low-order models applied to isolated and installed propulsors*), and the values of the local thrust coefficient extracted along each strip to produce an angular profile. Then an angular Fourier series is performed on each profile and transposed in the time domain

in the reference frame of the corresponding blade segment, providing the BLH of the segment. The procedure has been described by Roger and Moreau (2020), leading to the bar-plot in Fig. 3-b. The most striking feature is that BLH of orders ± 1 are generated with an amplitude of about 30% of the steady load (order 0). Stating that higher-order BLH are negligible is misleading, despite their much lower levels. Indeed, the weighting by the Bessel function acts as a filter on the BLH spectrum for each BPF harmonic. The most contributing BLH are those of orders $mB \pm n_m$, where n_m defines the bound of non-zero Bessel functions, the order $s = mB$ being the most efficiently radiating *a priori*. So, since $B = 2$, the BLH of order 2 is the most efficient, then those of orders 1 and 3, and so on. As a consequence, The order -1 can be ignored in the present case, whereas the order $+1$ is significantly contributing. Similar reasoning can be repeated for higher BPF orders. By the way, the steady loading can be found to contribute at the BPF but not at higher harmonics (see Roger (2022)).

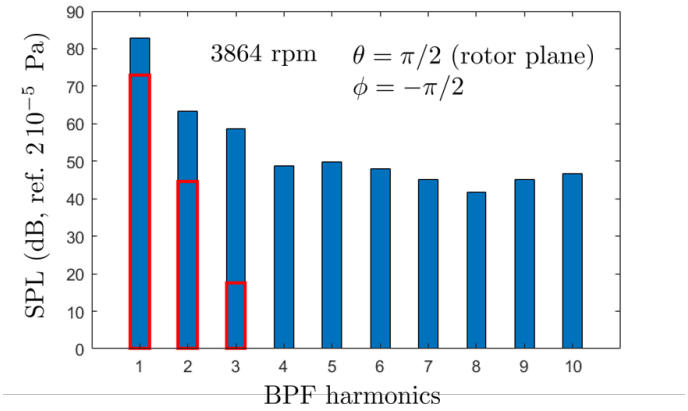


Figure 4: Indicative bar-graph spectrum of the tonal noise, as predicted from data in Fig. 3-b. Observation angles on the plot. Total noise (blue) and steady-loading noise (empty red).

Using the BLH deduced from Fig. 3-b as input in the far-field tonal-noise formula (see the lecture *Review of aeroacoustic analogies and applications to UAM*), the tonal noise can be predicted at arbitrary observation points. A typical sound spectrum is plotted as a bar graph in Fig. 4. Only retaining the term of order $s = 0$ also provides an estimate of the steady-loading noise, superimposed as the empty red bars on the plot. It appears that the tonal noise is essentially due to unsteady aerodynamics. Indeed, the first tone of typical drone rotors no longer dominates the spectrum once A-weighting is applied to get a better estimate of the annoyance. But because the data are extracted from the simulation of a complete quadrotor, it is impossible to decide about the relative contributions of edgewise flow and of rotor-rotor interactions. In the present case of quite low Mach number, the significant theoretical levels on a wide range of BPF harmonics is explained by the fact that the BLH of relatively large orders are made efficient by virtue of the Bessel-function factors, despite their low amplitudes in Fig. 3-b.

2.2 Potential Distortions and Wakes

Unsteady aerodynamics of blades systematically results from the presence of downstream or upstream obstacles, causing some local blockage of the ingested or rotor-induced flow. Downstream obstacles can be the air intake of a turboprop, as seen later on in Fig. 9, the front airframe of a light aircraft, the beam holding a rotor in a quadrotor drone architecture, an aircraft wing for a puller propeller, and so on. An upstream obstacle can be the pylon of a rear-fuselage propeller, or the wing and nozzles of the typical pusher-propeller arrangement of the Piaggio P-180 illustrated in Fig. 5 (see Marulo et al. (2005)). Blocking obstacles are responsible for a distortion of the surrounding mean flow, with respect to what would be obtained, were the propeller operating in totally open field with the same loading conditions. In particular, the fluid velocity drops in front of an obstacle, as drammatically as the considered point in the fluid is close to the stagnation point, as well as downstream.

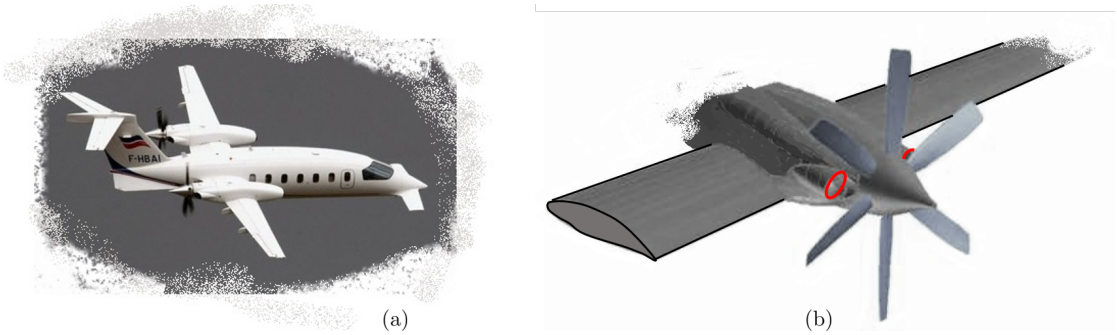


Figure 5: (a): Piaggio P-180 aircraft, picture from Internet. (b): pusher-propeller in the wake of the wing and in the exhaust jets of the engine, featured in red; artist's view.

Let's consider the case of the cylinder in a uniform flow normal to its span, as visualized in Fig. 6-a from numerical simulations reported by Jacob et al. (2014). The real flow upstream of the cylinder develops very similar to what a potential theory would predict. The streamline pattern, featured in green, is called a potential distortion. Unsteady separation takes place along the surface of the cylinder around some location, leading to the shedding of vortices in the wake, in the form of the so-called von Kármán vortex street. The viscous wake is made of a mean velocity deficit, characterized by a quite slow diffusion/attenuation. In contrast, the potential distortion extends only shortly upstream, strongly attenuating with distance. This explains why putting a rotor upstream or downstream of a cylinder-beam in a main stream *a priori* makes a major difference when the effect of rotor-beam distance is investigated (the mean lift on the blades also plays a role, as pointed later). As a first insight into the underlying physics, the contrarotating propulsive units pictured in Fig. 6-b would each correspond to a doublet of rotors, the front one of which operates through the potential-flow streamlines and the rear one through the wake. The front rotor only interacts with the potential distortion. Its contribution to the emitted sound is essentially tonal and is referred to as the potential-interaction noise (PIN). For it, slightly increasing the rotor-beam distance from a very short value results in a very significant decrease of the sound. The same can be transposed to the single-rotor units of most drones.

The mechanism by wich the rear rotors of the coaxial contrarotating pairs in Fig. 6-b generate noise is different, at least if the induced axial velocity is significant, in the sense that the wake of the beam is made of a mean velocity deficit and of a concentrated region of turbulence. Both tonal noise and broadband noise are generated. This is referred to as wake-interaction noise (WIN). For the downstream rotor, increasing the interaction distance, at least in a range of technologically acceptable values, could bring only minor benefit in the presence of high axial flow. But still another mechanism must be considered in the contra-rotating system, namely the interaction of the wakes shed from the upper rotor with the blades of the lower rotor, referred to as rotor-rotor wake-interaction noise. In the same way, the potential field of the lower rotor could induce fluctuating loads on the blades of the upper rotor for short vertical separations. The aeroacoustics of contra-rotating systems appears as very intricate, especially in the presence of a supporting beam. It is only mentioned here for completeness, but will not be addressed in the lecture, for conciseness. Let's just point that Huff et al. (2021) observed that the bottom rotor of a unit of the Moog SureFly aircraft produced much more sound that the top rotor. A parametric study, focused on small contra-rotating systems, can be also found in the work by Chaitanya et al. (2022).

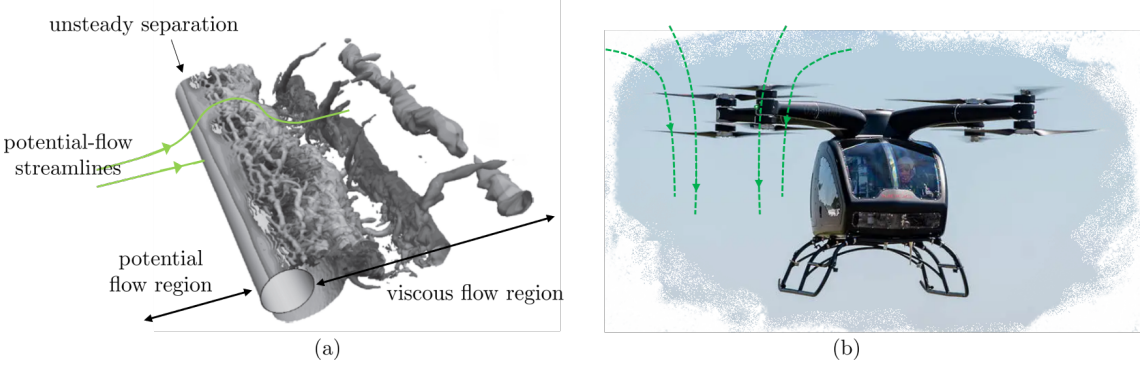


Figure 6: (a) structure of the flow around a cylinder, from Jacob et al. (2014). (b) example of pairs of contrarotating rotors mounted upstream and downstream of a central beam, on the Moog SureFly aircraft. Ideal mean streamlines of the induced flow, ignoring distortion, featured in green (see also Huff et al. (2021)).

This analysis is based on an ideal view of wakes and potential distortions, whereas recent numerical simulations reveal more subtle intricate mechanisms. For instance, adding a rotor at very short distance in the upstream region of the cylinder considered as beam in Fig. 6-a induces strong disturbances also on the front face of the cylinder, possibly inducing unsteady separation triggered by the blade passages, as suggested by numerical simulations reported by Rendon et al. (2024) and as confirmed by Gojon[4]. Furthermore, the potential flow field around the cylinder is upstream/downstream symmetrical, which

[4]R. Gojon, personal communication. Note that the natural vortex shedding of a cylinder requires ideal conditions and a large-enough aspect ratio. It is not likely to take place in the case of rotor-beam interaction. Indeed, firstly, the Reynolds number can enter its critical range of values (on eVTOL aircraft), for wich only random motion in the wake is obtained. Secondly, the flow pulsations are imposed by the blades.

means that what is referred to as wake interaction for a downstream rotor at short distance is in fact combined with potential interaction. True WIN dominates in rotating-blade technologies operating in a well established axial mean flow.

Obviously, in the rotor-beam system, strong aerodynamic sound sources are also developing on the surface of the beam. In fact, the configuration is similar to a rotor-stator stage that would only have one non-profiled vane. Moreover, recent studies establish that the beam contributes to the tonal noise, more than the rotor itself, even though it is a stationary surface.

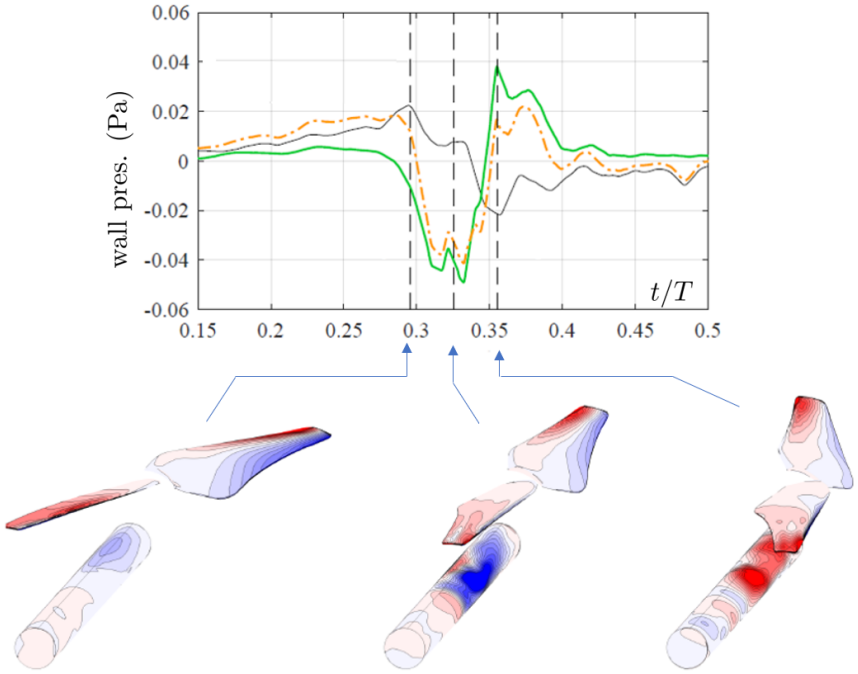


Figure 7: Instantaneous surface-pressure distributions on the cylinder and blades of the configuration simulated by Zawodny and Boyd (2019), as well as pressure signals recorded at a microphone located at oblique position downstream. Cylinder alone (green), rotor alone (black) and complete system (orange dotted).

Very meaningful observations were reported by Zawodny and Boyd (2019), who analyzed numerical simulations of the flow around a rotor-cylinder arrangement and post-processed the surface pressures by the acoustic analogy to get the acoustic pressure at a far-field point. Key results are reproduced in Fig. 7. Instantaneous surface-pressure patterns on the rotor and cylinder surfaces are shown, for 3 time steps also pointed on the sound-pressure signal, in terms of time relative to the period t/T. The post-processing allows to separate or combine the respective contributions from the two surfaces. The dominant source is seen on the cylinder, but its sound interferes with that of the rotor to produce a modest, but not negligible, cancellation. This stresses the intricate character of the involved sound-generating mechanisms, on the one hand, and the questionable relevance of separating surfaces which contribute coherently, on the other hand.

A similar study was recently reported by Gojon et al. (2023) and Vella et al. (2024),

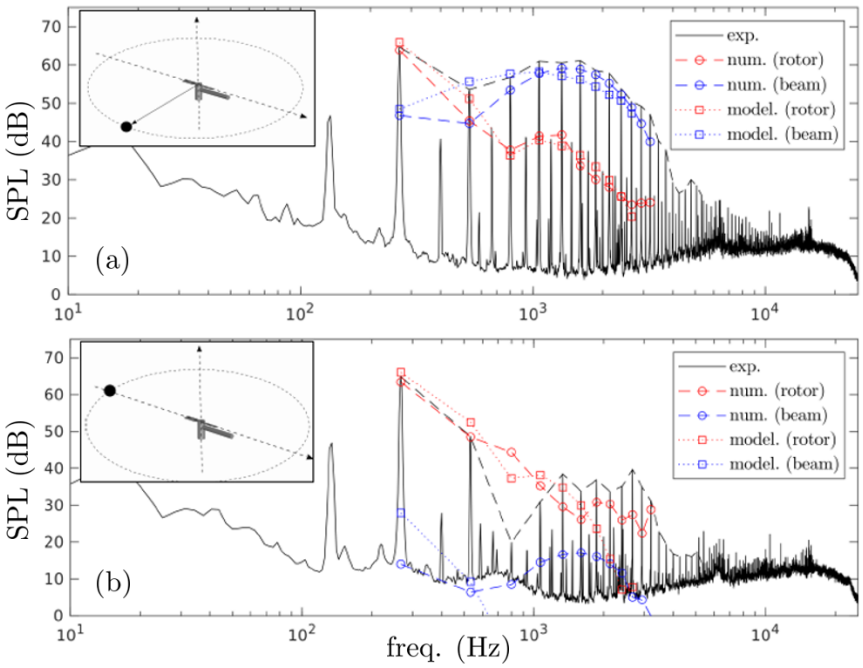


Figure 8: Sound spectra measured on the rotor-beam setup of Vella et al. (2024) (black), and accompanying predictions of the tonal noise, with separate contributions from the rotor (red) and from the cylinder (blue). (a): microphone at 90° to the cylinder axis; (b): microphone on the cylinder axis.

who confirmed that the cylinder is the dominant source, relying on both experiment and modeling, at least in some conditions and at some frequencies. Sample results are presented in Fig. 8, for two microphone positions close to the plane of the rotor, made of NACA-0012 blades. The numerical predictions are obtained with a post-processing of incompressible LES by the acoustic analogy, which allows to separate the contributions from the rotor and from the beam. The analytical predictions will be discussed in the lecture *Semi-analytical and low-order models applied to isolated and installed propulsors*. Two major comments can be made to complete the analysis of the interaction. Firstly, the first BPF tone emerging with high amplitude is known to be dominantly attributable to steady-loading noise and, as such, does not involve the cylinder. Only higher-order tones are associated with the flow distortion. Secondly, the source ranking depends on the observation angle. For an angle of 90° with respect to the cylinder (Fig. 8-a), the sound is essentially emitted from the cylinder (note that the rotor plane is most often close to a local minimum of rotor tonal noise). But for an observer along the cylinder axis (Fig. 8-b), the cylinder no longer contributes because this is the direction of extinction of the dipoles of its unsteady-loading noise.

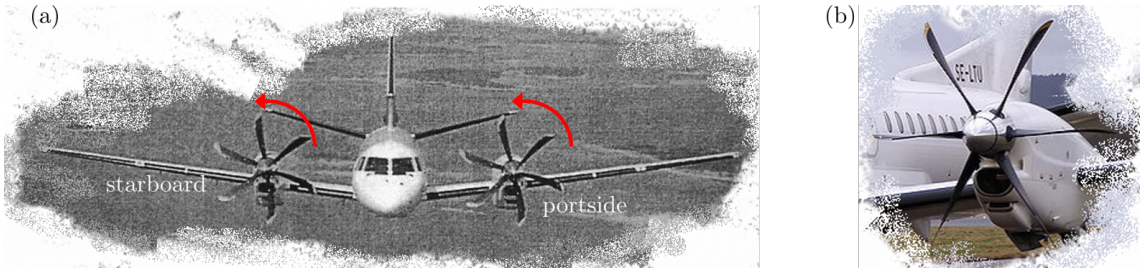


Figure 9: (a) front view of the SAAB-2000 aircraft. (b): close-up on the turboprop air intake.

2.2.1 Case Study: the SAAB-2000

This section describes the illustrative example of the air intake of the turboprops of the SAAB-2000 aircraft, initially found to be the cause of detrimental tonal noise, and reported by Leth et al. (1998). This example is also discussed in a previous lecture series of the VKI[5], only key aspects are given in this section. When seen from upstream, the aircraft is powered by two counterclockwise rotating propellers, on each side of the fuselage (see Fig. 9). For the study, wall microphones were flush mounted on each side of the fuselage. A much higher sound was measured by the starboard microphone, associated with a strong impulse, compared to the portside, as shown in Fig. 10-a. Tonal noise spectra provided by Fourier series of the signals are plotted in Fig. 10-b. The impulse in the time domain corresponds to a much higher sound, and a richer harmonic content, in the frequency domain. The overall difference exceeds 15 dB. The authors identified the potential distortion of the flow around the lips of the intake as the origin of the impulse. Indeed, as seen in Fig. 9-b, the blades obviously experience a strong variation of angle of attack when crossing the distortion, because of their close vicinity to the lips. The

[5]M. Roger, Aeroacoustics of installed propellers, in VKI LS *Aircraft electric propulsion, EAC 1804*, 2019

simple solution implemented by SAAB was to increase the length of the shaft by a couple of centimeters. This was found enough to prevent the strong interaction related to the impulse, taking benefit from the very rapid decay of the potential distortion upstream of obstacles.

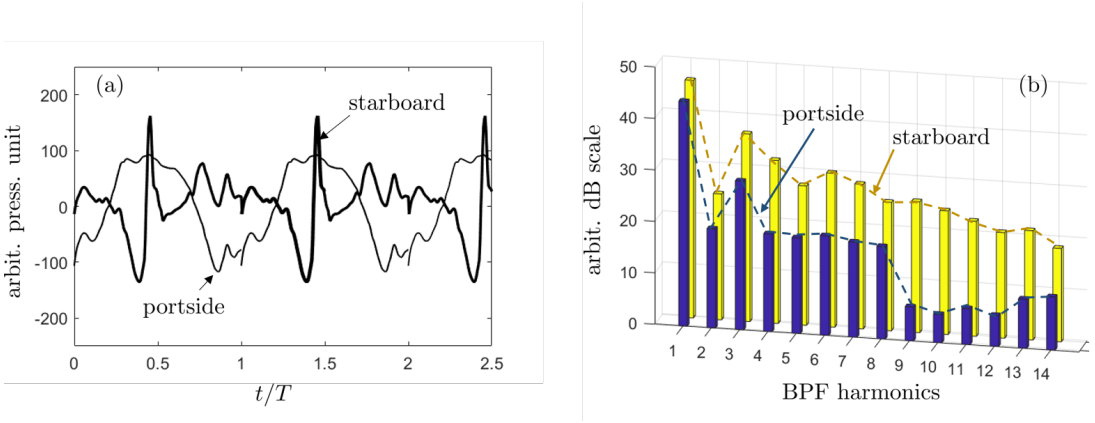


Figure 10: (a) Microphone signals on both sides of the fuselage of the SAAB-2000 aircraft, reported by Leth et al. (1998). (b): corresponding tonal-noise spectra.

The initial imbalance between signals on both sides of the fuselage is explained by the impulsive signature of the potential interaction with the intake lips, on the one hand, and by the fact that both propellers rotate in the counterclockwise direction, on the other hand. Indeed the contribution from a compact blade segment, in particular the one crossing the intake distortion, reads in the form

$$p(\mathbf{x},t) \;=\; -\frac{1}{4\pi\, c_0}\left[\frac{R_i}{R^2\,(1-M_r)^2}\,\frac{\partial F_i}{\partial \tau} - \frac{R_i F_i}{R^2\,(1-M_r)^3}\,\frac{\partial M_r}{\partial \tau}\right],$$

if M_r denotes the source-motion Mach number relative to the observer and $\mathbf{F}$ the dipole strength vector. The squared brackets stand for the evaluation at the emission time. Because the distortion is localized, the maximum $\partial F_i/\partial\tau$ occurs as the blade segment of the starboard propeller approaches the fuselage, but also as the portside propeller retreats away from the opposite side of the fuselage. Even for a subsonic Mach number, the amplification brought by the term $(1-M_r)^2$ in the denominator focusses the emission in the direction of motion of the blade. This induces a difference of sound amplitude in the ratio $(1+M_c)^2/(1-M_c)^2$ between starboard and portside microphones, if M_c denotes the tangential Mach number of the blade segment at the moment of interaction. This is why the starboard propeller radiates dominantly towards the fuselage, whereas the portside one radiates towards the wing tip, a much more silent configuration for passengers. For the segment of interest, the term $\partial M_r/\partial\tau$ contributes at a much lower, negligible level, as long as $\partial F_i/\partial\tau$ is strong.

2.3 Propeller-Wing and Propeller-Pylon Interactions

Whatever they are used in conventional or innovative architectures, such as in eVTOL aircraft, puller propellers operate upstream of the wing or pylon on which they are

mounted. This generates other interactions, in the continuation of the aforementioned effect of engine inlets and supporting beams. Not only the leading edge of the wing causes blockage of the flow, but also its quite large surface makes it an additional source of noise, by impingement of the propeller slipstream. The investigations by Mukherjee and Brentner (2020) and Zawodny et al. (2021) are cited here as examples of recent reference works.

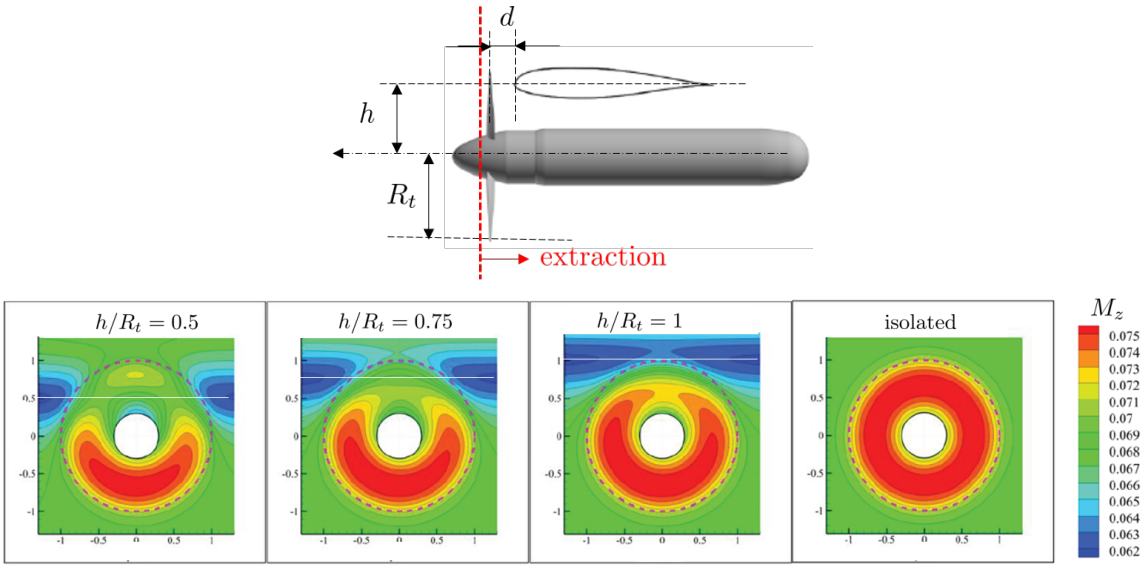


Figure 11: Side-view of the propeller-wing arrangement investigated by Zawodny et al. (2021), and axial-flow Mach-number maps in the extraction plane, for values of wing height h.

Figure 11 refers to a propeller-wing system possibly mimicking installed propulsive units of tilt-rotor concepts. The axial and vertical distances of the propeller disc and axis to the wing leading-edge, noted d and h, are varied in the test matrix. The features of the potential flow distortion are illustrated by extracting the axial Mach number from numerical simulations, in a plane parallel to the propeller disc and located 0.15 R_t upstream. In the figure, the vertical position of the leading edge is indicated by the white horizontal lines. The significant drop of axial-flow velocity is clearly seen, of about 12%. The associated variations of angle of attack on the blades generate lift fluctuations, radiating as dipoles. For comparison, the perfectly axisymmetric map of the isolated propeller is also shown. This case corresponds to constant blade forces, thus steady-loading noise only. It is the minimum-noise configuration.

2.3.1 Case Study: the ENODISE B2 Configuration

A sub-system of the configuration B2 of the ENODISE project is mentioned here as an example, the complete experimental setup being described in section 3.3. The sub-system is made of a propeller with an axisymmetric center-body mounted in front of a radial, NACA-shape pylon. It is shown in Fig. 12. The pylon has the same effect of a wing, except that it only extends over half the diameter. Its thick and rounded leading edge causes

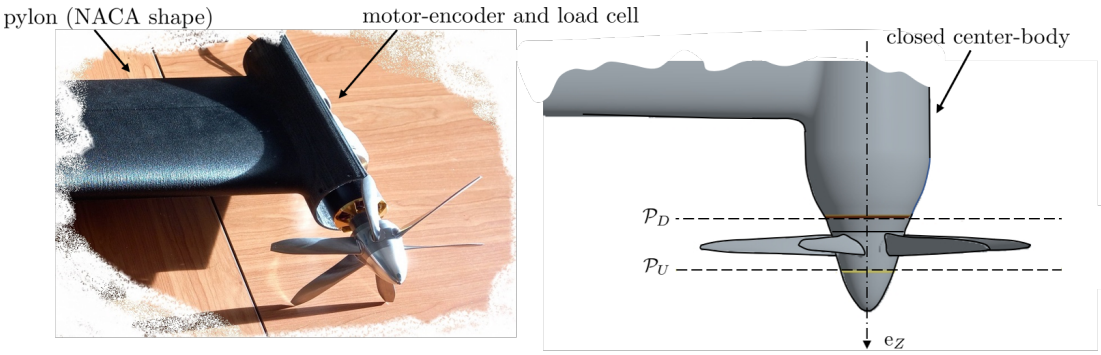


Figure 12: Propeller-pylon unit of ENODISE project, configuration B2, wing removed, and definition of extraction planes in numerical simulations.

potential distortion. In complement to the experimental investigation in the project, numerical simulations have been performed on an isolated unit, for the two values 0 and about 0.95 of the advance ratio. In the latter case, discussed first, the free-stream velocity is 22 m/s and the rotational speed is 7,000 rpm, for a blade-tip radius of about 10 cm. Computed mean-velocity components were extracted in two discs, positioned upstream ($\mathcal{P}_U$) and downstream ($\mathcal{P}_D$) of the propeller disc, as shown in Fig. 12 (see LeBras et al. (2024)).

Results are reported in Fig. 13. As expected for an axial-flow technology, the maps of radial velocity components are almost perfectly axisymmetric, showing low values. In contrast, large distortions are noticed on the other two components. The flow blockage by the pylon, the angular position of which is indicated by the gray bar, is clearly identified on the downstream axial-velocity map, Fig. 13-f. But a significant tangential-velocity distortion is seen upstream, Fig. 13-b. This corresponds to the upward and downward fluid motions needed to go around the pylon. The distortion is still significant, despite the quite large distance seen in Fig. 12-right, compared to the configuration of Zawodny et al. (2021). It has been found responsible for most of the tonal noise radiated by the complete system, including two synchronized propellers and a wing (section 3.3). This test case will be re-addressed in the lecture *Semi-analytical and low-order models applied to isolated and installed propulsors*. For information, typical sound spectra of the complete system are given in Fig. 14, at advance ratios 0 and 0.95 but at the same rotational speed, and for two microphones located in the propeller plane, perpendicular to the flow and on each side of the system. A much higher noise, both tonal and broadband, is observed at zero advance ratio, because the loading conditions on the blades are much stronger. The tone at the BPF cannot be explained by steady-loading noise on a 6-bladed propeller, unlike the previously discussed case of 2-bladed drone rotors, by virtue of the Bessel-function weighting. The potential interaction is the incriminated mechanism.

Figure 15 shows a reduced set of results, focusing on a single propeller-pylon unit (wing removed), at the zero-advance ratio regime, and comparing measured and predicted spectra. At the tip Mach number of 0.2 of the test case, LES is performed and post-processed by the procedure of LeBras et al. (2024), allowing to separate source and scattering contributions. For a relevant comparison with the experiment, the bandwith achievable in the simulations is selected, reducing the resolution to 58 Hz. The BPF har-

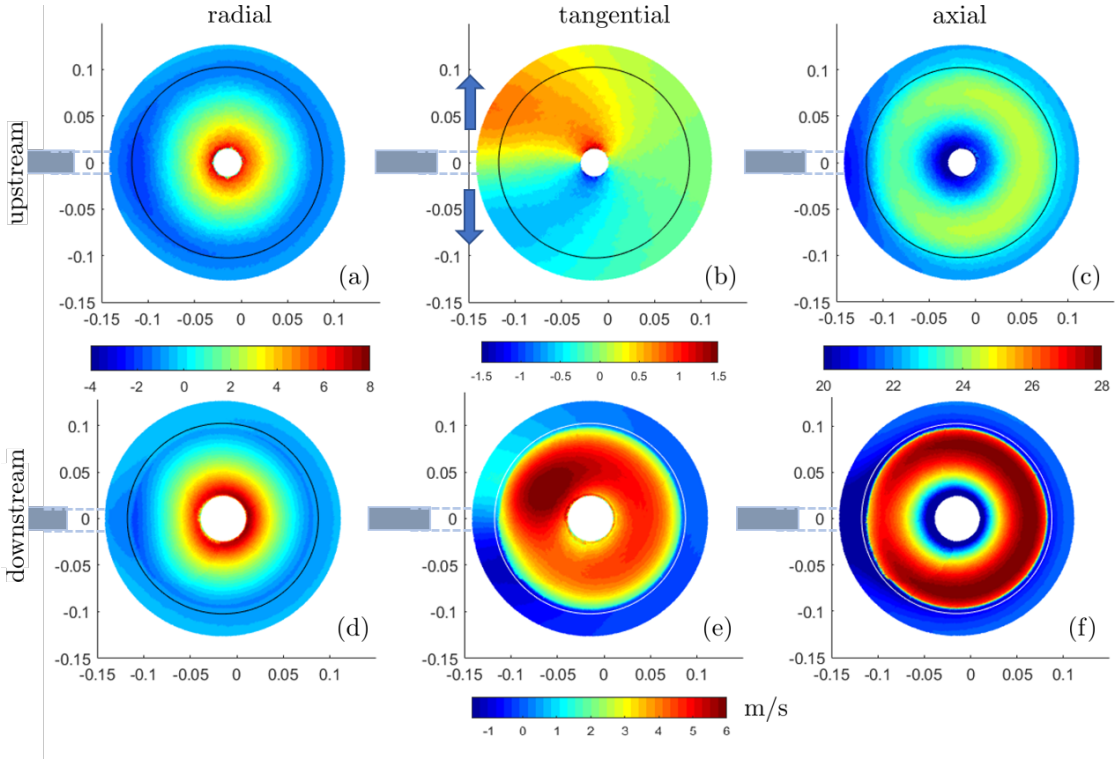


Figure 13: Typical mean-flow component maps in upstream and downstream extraction discs around a propeller-pylon unit. ENODISE project configuration B2, wing removed. RANS simulations, courtesy of Siemens Group.

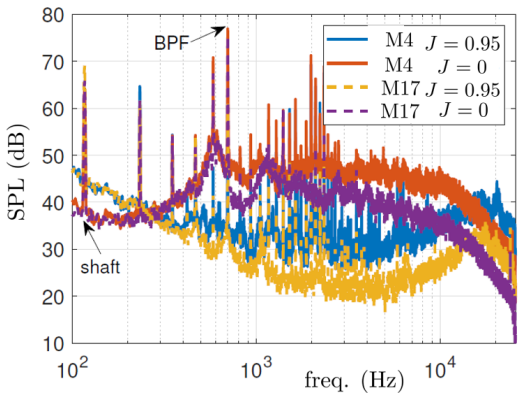


Figure 14: Measured sound spectra of the ENODISE configuration B2 at advance ratios 0 and 0.95, from Acevedo Giraldo et al. (2023). Complete setup and microphone positions given in section 3.3.

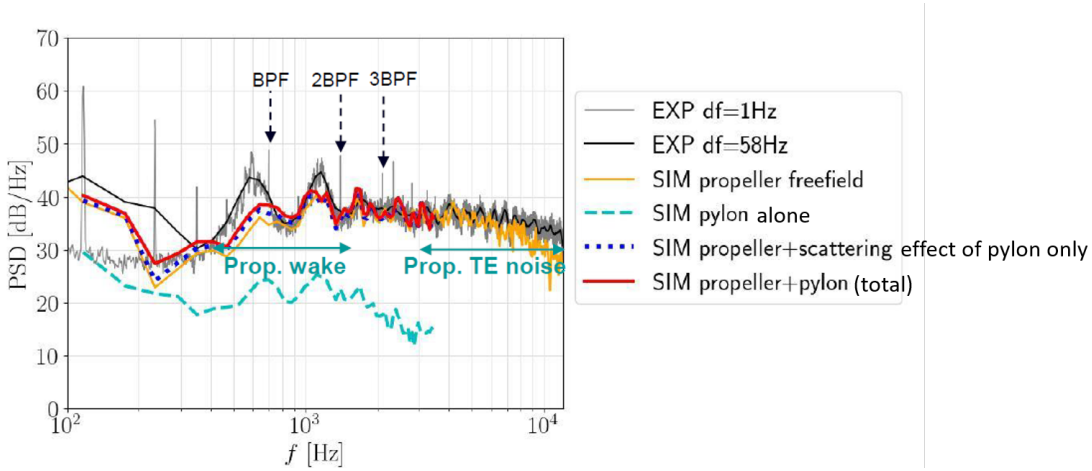


Figure 15: Sound spectra of the propeller-pylon unit of ENODISE project, configuration B2, at zero advance ratio, from LeBras et al. (2024). Measured spectra(EXP) versus simulated contributions (SIM).

monics cannot be precisely tracked, but a very good overall agreement is obtained. The ranking of mechanisms is reliable. At zero advance ratio, the blade-tip vortices cannot be evacuated in the main stream and stay around the propeller plane, with their intrinsic unsteadiness, slightly drifting azimuthally. They are cut by the blade tips at a reduced relative tangential speed, which generates the humps at frequencies lower than the BPF harmonics. In this case, the induced velocity is the only motion towards the pylon. The noise is dominantly radiated by the propeller, with some scattering effect of the pylon, of only a couple of decibels.

2.4 Boundary-Layer Ingestion

A new aircraft concept called BLI (Boundary-Layer Ingestion) consists in designing partly buried engines in the airframe, in order to reduce the front surface and the total drag. The principle is to ingest the velocity deficit in the boundary layers developing along the fuselage, in order to fill the deficit in the wake. But apart from the expected higher propulsive efficiency and lower fuel burn, acoustic issues are raised. The flow ingested by the fan or propeller partly immersed in the turbulent boundary layer is highly distorted, which is known as a source of unsteady loads on the blades, thus tonal and broadband noise. Examples of BLI concepts are the ONERA NOVA, the MIT-Aurora-P&W D8, the NASA N3-X, the propulsive rear-fuselage, reviewed by Moirou et al. (2023). No detail of this specific interaction are given here, but key features can be expected [6].

[6]BLI is the matter of the ENODISE project Configuration A, databases being available on Zenodo.

3 Acoustic Installation Effects

3.1 Scattering by Fuselage and Airframe

As previously stated, acoustic installation effects refer to modifications of the radiating properties of sound sources caused by neighboring surfaces, not considering changes of the sources themselves. This means, for instance, that they can be predicted by any propagation solver, based on the Helmholtz equation or on linearized Euler equations (LEE), starting from specified sources. More fundamentally and prior to any accurate prediction, dimensional analysis provides a useful *a priori* ranking of expected trends. For this, the involved characteristic length must be listed and estimated. Indeed, diffraction/scattering is a matter of compared geometrical scales and acoustic wavelength λ. Obvious parameters, apart λ, are the source distance to the scattering body, and more especially the distance to singular points of this body, as well as its size.

A first commonly encountered case is that of the scattering of propeller noise by the fuselage of an aircraft. For large-enough aircraft and puller propellers, such as the ones of the SAAB-2000, some masking effect is expected: the sound from the starboard propeller is minimum on the portside, and *vice versa*. But this is so only as long as the diameter of the fuselage, say D_f, exceeds λ for the frequencies of interest. Let's take as hypothetical but realistic values a source radius of 1.2 m, a diameter D_f of 3 m and a Mach number of a segment of 0.7, for a 6-bladed rotor. The BPF is about 190 Hz, corresponding to $\lambda \simeq 1.8$ m. Efficient masking is expected in such a case, more pronounced at higher harmonics of the BPF. But the blade-tip radius also plays a role; sources at some positions along the circular path of a blade segment can regenerate sound in the shadow region of diametrically opposite sources. Up to that point, the example of the passenger aircraft is a non-compact case. Different behavior is expected for other sets of parameters. Quite generally, dimensional analysis should be attempted in any addressed configuration, as a guideline for relevant approximation and for ranking of mechanisms.

Another topic of interest is the possible masking of the noise of a propulsive unit by the airframe, understood as a potential benefit of diffraction. Essentially, the most effective masking is expected from surfaces of large extent, such as the wing and tail of a passenger aircraft. Some breakthrough architectures try to maximize it, for instance the blended wing-body concept, versions of which are illustrated in Fig. 16. A very substantial masking is expected for the sound radiated by propulsive units installed above the fuselage, as reported by Guo et al. (2014). It is worth noting that the version of BWB in Fig. 16-b also involves the typical aerodynamic installation effect of BLI: the boundary layer developing along the top fuselage is ingested by the engines, generating a significant distortion for the fans.

3.2 Compact Scattering

3.2.1 Short Review of Previous Works

Special behaviors have been reported many times in the literature in configurations for which a source of sound is approached at very short distance to a geometrical singularity or to a small scattering body. Here, very short and small mean much smaller than the acoustic wavelength of interest. Such cases are referred to as the compact regime of

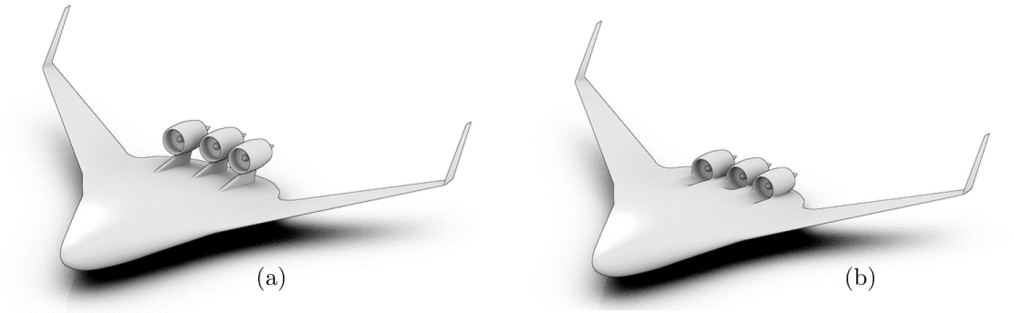
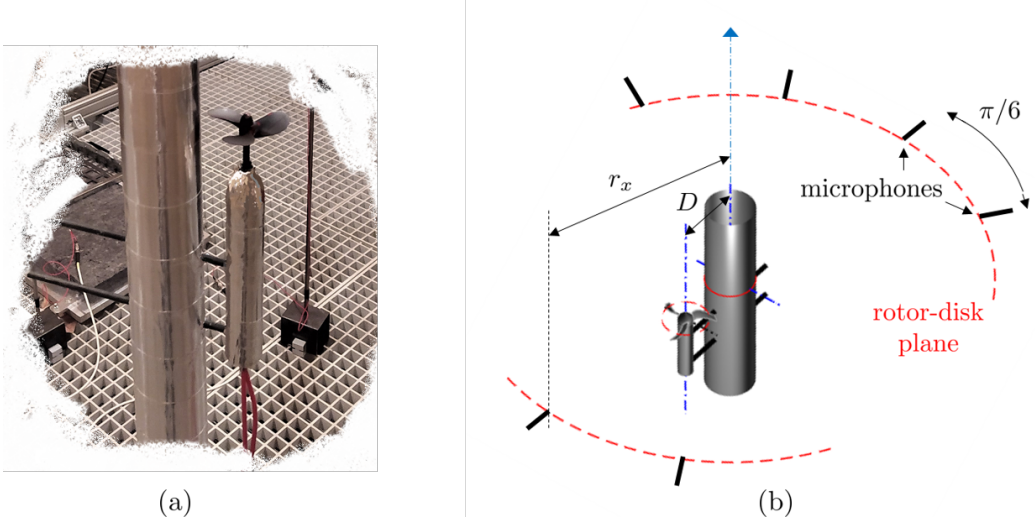


Figure 16: Pictures of the blended wing-body concept assessed in the AGILE project, from project Website. Conventional engines on pylons (a), and BLI version (b).

scattering/diffraction in this lecture. In this regime, typically, the scattering surfaces strongly modify the radiation from sources of high polar order, resulting in both global amplification and restructuration of the directivity. Basic examples are shortly reviewed in this section, prior to applications in rotating-blade noise technology.

The first example is the scattering of quadrupoles by the edge of a rigid half-plane, formulated by Ffowcs Williams and Hall (1970) to model the scattering of boundary-layer turbulence as sound at a trailing edge. Indeed, following Lighthill's analogy, turbulent mixing is equivalent to quadrupoles, the radiation of which is calculated by solving Lighthill's equation. In the present case, use is made of the half-plane Green's function for this. The scattering of turbulence into sound takes place in a very compact area around the edge, which is exactly the framework of the compact regime. Amplification of the sound pressure from the quadrupoles was found, proportional to $(kr_0)^{-1}$, if k is the acoustic wavenumber and r_0 the distance to the edge. This explains why the direct sound radiation from a developed turbulent boundary layer over a flat or smooth wall remains very poor, whereas a much higher sound is emitted from the trailing-edge area. An extension of the analysis to dipole sources in the presence of a uniform mean flow was proposed by Roger et al. (2016) to model the diffraction of flap noise by the trailing edge of a wing, understood as a low-frequecy mechanism in high-lift device noise. The amplification was found proportional to $(kr_0)^{-1/2}$.

The second example is the scattering of a quadrupole by a rigid cylinder, addressed numerically by Gloerfelt et al. (2005) to interprete the vortex-shedding sound from a cylinder in a flow. The formation of the closest staggered vortices was found equivalent to a lateral quadrupole, and the configuration highly compact at the low investigated Mach number. In such conditions, the scattering by the cylinder produced a high-amplitude lift-dipole pattern, totally different from what the quadrupole would have radiated in free field. More recently, compact scattering by a cylinder was addressed by Cros et al. (2023), considering as source a very small three-bladed propeller. The study was experimental and analytical. Propeller and cylinder axes were parallel, and the parameters were such that the global area encompassing the propeller and the cross-section of the cylinder was acoustically compact (see Fig. 17-a). In fact, the investigated Helmholtz numbers were rather representative of marine propellers. Measurements were made in the far field with



(a) (b)

Figure 17: Acoustically compact setup investigated by Cros et al. (2023). (a): picture of the propeller-cylinder arrangement. (b): positioning of the array of microphones for modal projections.

a circular array of microphones, in order to expand the acoustic field as spinning modes in the plane containing the propeller disc, as shown in Fig. 17-b. In this experiment, azimuthal distortions of the flow through the rotor disc are negligible or at residual level, because the cylinder causes no blockage of the propeller downwash. This suggests that the emitted sound is essentially steady-loading noise, associated with the rotor-locked mode $n = 3$. Indeed, this mode was detected as dominant by the array when the cylider was removed, as reported in Fig. 18-a. As the cylinder was approached at very short distance to the propeller, a much higher sound was heard at the BPF. The key finding was that the total field was now dominated by the scattered field from the cylinder, essentially made of the mode -1. This unexpected result was reproduced analytically with an asymptotic analysis of a model, described in the lecture *Semi-analytical and low-order models applied to isolated and installed propulsors*.

A similar effect is probably observed in the rotor-beam configurations of small-size drones, and contributes to the increase of sound as the rotor-beam distance is reduced. Indeed, the same short distances between sources and scattering surfaces are encountered, except that now the cylinder and source-mode axes are perpendicular to each other. This point will be also discussed in the lecture dedicated to analytical modeling.

The main general idea is that, in some conditions, compact scattering changes the basic radiation of high-polar order sources into that of 1-degree lower order sources, thus much more efficient. Going into details, the cylinder does not amplify the radiation of dipoles, unlike what is observed with the half-plane. As long as described in a two-dimensional context, these basic facts can be related to the formalism of compact Green's functions proposed by Howe (2003).

3.3 Case Study: ENODISE Configuration B2

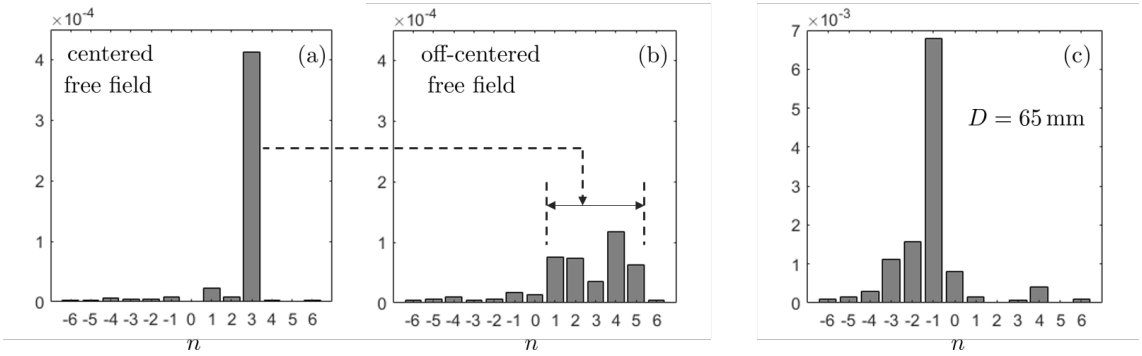


Figure 18: Modal spectra at the BPF, processed from the sound field of the small propeller shown in Fig. 17. Free field with propeller centered (a) and off-centered (b) in the circular microphone array. (c): total field with the cylinder at minimum distance D.

The configuration B2 in ENODISE project was aimed at primarily assessing the acoustic installation effect expected as a pair of side-by-side synchrophased propellers are installed over a lifting wing (see Acevedo Giraldo et al. (2023)). The varied parameters were the propeller-propeller distance, the relative phase between the propellers (either 0 or 30° corresponding to half a blade passage), and the streamwise and normal distances to the trailing edge, for two advance ratios, namely 0 (static operation) and 0.95 (main stream speed delivered by the wind tunnel of 22 m/s) [7]. The setup, shown in Fig. 19, is designed with movable pylons attached to a vertical mast separated from the wing-and-nozzle assembly, in order to avoid the transmission of mechanical vibrations. The wing can slide vertically through slits in its two mounting supports, featured in light brown in Fig. 19-a. The latter are narrow enough to enable one to perform acoustic measurements at elevation angles off the (horizontal) mid-span plane, with negligible spurious sound reflections. Moving the wing also allows to construct a map of the pressure coefficient C_p, with only two chordwise lines of pressure taps. Indeed, the presence or the positioning of the propellers modifies the C_p distribution, thus the total lift of the wing; this must be considered as part of the aerodynamic installation effect. In contrast, it was verified that the blade tips were not interacting with the wing boundary layer, except for the very tip area and the shortest wall-propeller distance. This prevents the generation of significant BLH, only residual fluctuations resulting from the operation in the general mean-flow acceleration over the wing suction surface. The expected dominant source of BLH is in the potential distortion of the flow around the pylons, not very different in installed and uninstalled configurations. Finally, the B2 setup is well-suited to investigate the acoustic effect on the noise of a propulsive unit caused by the wing, the unit being defined by the propeller and its pylon-and-hub, featured in black in Fig. 19-a.

Key results for the tonal noise at the BPF are summarized in Fig. 20, in terms of three-dimensional maps on the part of observation sphere covered by the antenna. The black dots stand for the measuring positions. As shown by the first plot for the free-field

[7]The complete database is available on Zenodo, at the address Acevedo-Giraldo D., Roger M. & Jacob, M.C., H2020 ENODISE: Experimental dataset configuration B2 ECL, https://zenodo.org/record/7925336, 2023. More complete results are found in the PhD thesis by Acevedo Giraldo (2024)

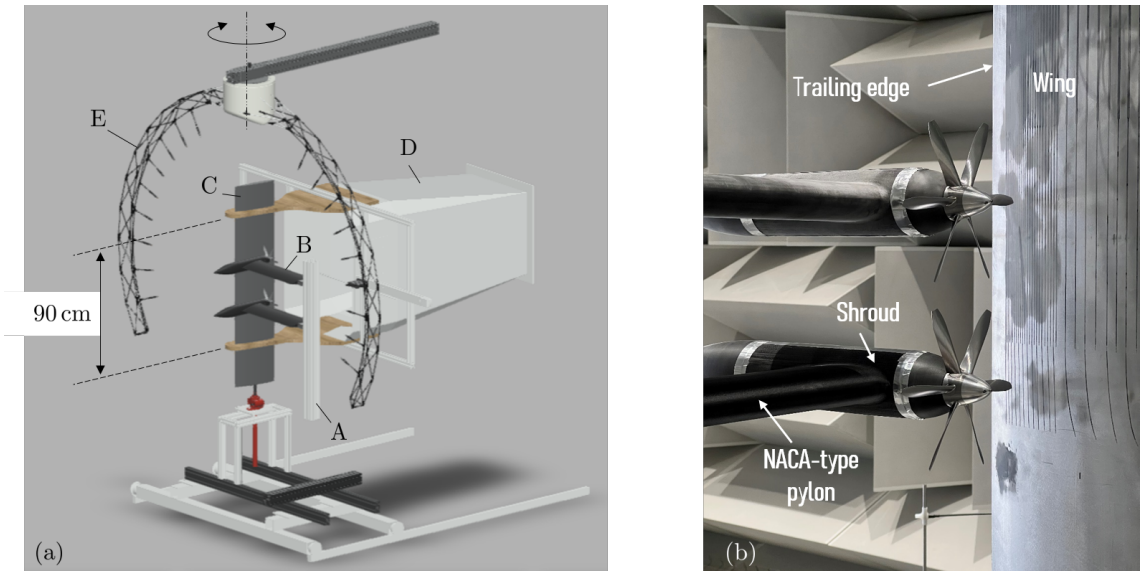


Figure 19: Experimental setup of the Configuration B2 of ENODISE, tested at ECL. (a): general CAD view. A: mast supporting the two propeller units (B); C: wing; D: diverging duct of the wind tunnel; E: arc-antenna of microphones. (b): picture of the two pylon-propeller units.

with the minimum propeller-propeller distance (21 cm axis-to-axis, corresponding to 5 mm tip-to-tip) and the 30° relative phase (Fig. 20-a), a higher sound amplitude is found on the right side of the map (left-bank side of the wind tunnel). This is because the propellers are displaced from the center of the observation sphere, for installation constraints of the setup (see Fig. 19). When adding the wing, with the same pair of propellers installed close to the edge in terms of both streamwise and normal distances, a strong increase of sound level is observed, on both sides, wheras some masking (moderate in this case) would be expected on the left side (right bank). This is the declination of the aforementioned compact scattering operating on the special case of tonal-noise source-modes. The latter are somehow equivalent to higher-polar order sources. In contrast, as the propellers are installed farther away from the edge as in the case of Fig. 20-c, efficient masking is found on the righ-bank side, with some reflection on the left-bank side, as expected from simplistic geometrical arguments.

Repeating the comparison on the broadband noise content, integrated over the range 4-to-24 kHz, after filtering out the tones, leads to the results in Fig. 21. Now the free-field configuration radiates almost symmetrically, keeping in mind that the propellers are closer to the left-bank side. Furthermore, the two installed configurations have similar acoustic signatures, free of amplification, featuring efficient masking on the right-bank side (left) and re-inforcement by reflection on the left-bank side (right). Amplification by compact scattering is only observed on modal patterns, not on uncorrelated sources. Furthermore, broadband noise is considered in a range of relatively high frequencies here, for which the compact scattering regime is probably avoided.

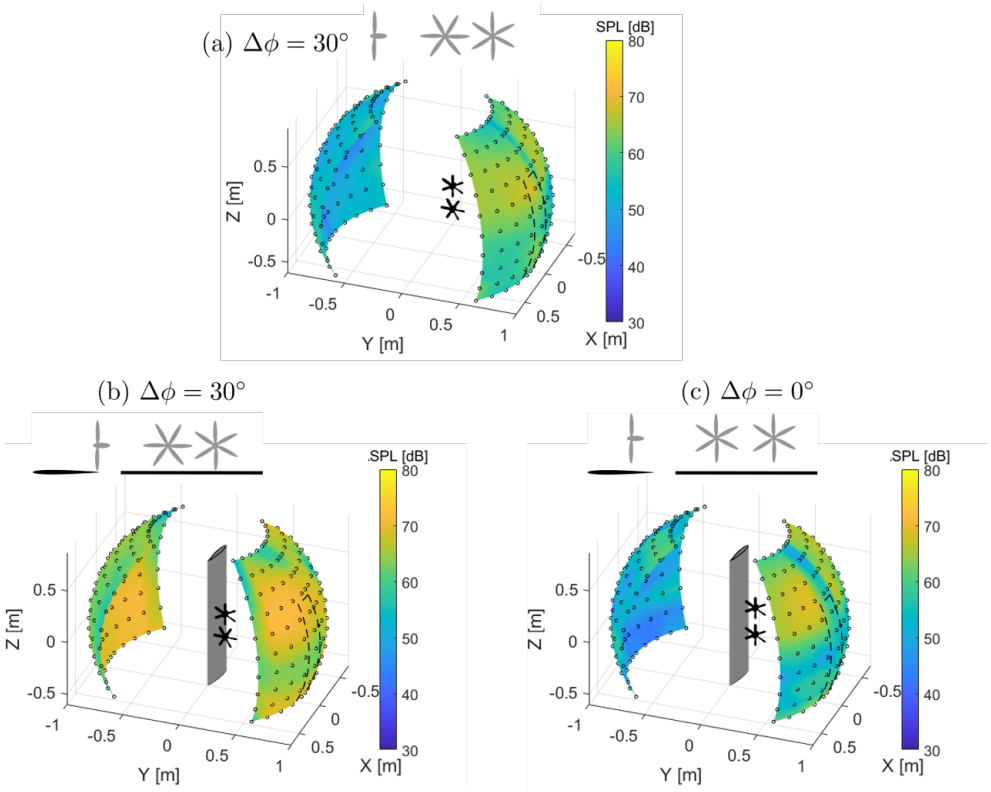


Figure 20: Three-dimensional SPL maps at the BPF measured in the ENODISE project, viewed from oblique downstream, for two propeller arrangements. 30° (a-b) or zero (c) relative phase, shortest (a-b) or largest (c) prop-prop distance. Configurations of compact scattering with amplification (b), and of efficient masking (c). Small schematic side and front views added above each plot.

3.4 Case Study: the Shrouded Tail Rotor

The diffraction caused by the short shroud of a helicopter tail rotor is a topic of interest, in view of its similarity with some propulsive units of eVTOL aircraft concepts. It was addressed by Roger and Kucukcoskun (2019) with a FEM solver, focusing on source-modes of the tonal noise produced by potential interaction with the transmission shaft. A simplified mesh was defined, according to the comprehensive sketch in Fig. 22. Typical results are reproduced in this section to stress the importance of scattering, even with a short casing.

Figure 23 displays SPL maps in the meridian plane (Y, Z), comparing the free-field radiation of sources at the mid-span radius (left) to their total field in the presence of the shroud (right). The source-mode parameters are given in the reference, the example is only given for illustration. Tones at the BPF and at 3BPF are considered, at 2920 rpm. The main dimensions of the shroud are indicated in the figure, to be compared to the wavelength at BPF, close to 70 cm. Most cross-section dimensions are nearly compact at this frequency, but no longer at the higher harmonic. Two lobes are seen at the BPF (top plots), with focussed oblique radiation in the quadrant $Z < 0$. The effect of the shroud is just to tilt the lobes towards the axis and to force secondary lobes in the quadrant $Z > 0$,

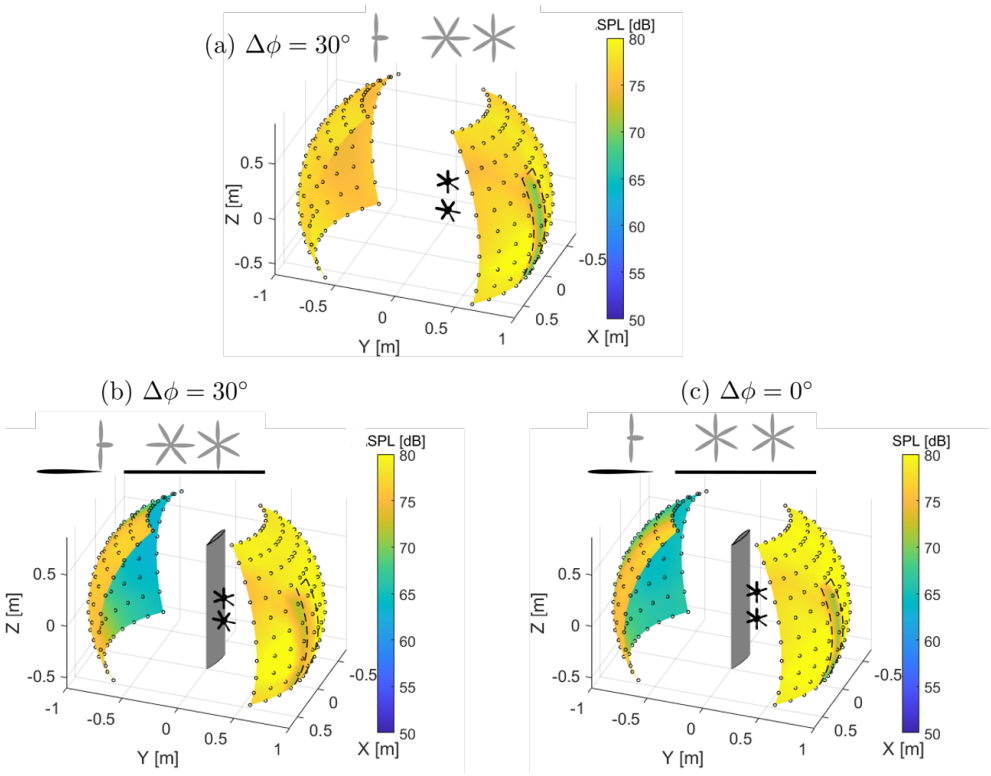


Figure 21: Three-dimensional SPL maps of the broadband noise (4-24 kHz) measured in the ENODISE project, viewed from oblique downstream, for two propeller arrangements. 30° (a-b) or zero (c) relative phase, shortest (a-b) or largest (c) prop-prop distance. Same configurations (b) and (c) as in Fig. 20. Small schematic side and front views added above each plot.

but globally the same energy is radiated. More complicate patterns are seen at 3BPF, a frequency for which the wavelength (about 23 cm) is of the same order of magnitude as the width of the shroud (20 cm). The free field is no longer axisymmetric, because of the modal content, not detailed here, and exhibits two lobes in the upper part, and a weaker third one in the lower part. The main lobe radiated normal to the rotational axis was found to be dominated by the mode $n = 8$ in the paper, whereas the oblique lobe at 45° in the quadrant $Z < 0$ corresponds to the mode $n = 3$[8]. Adding the shroud increases the number of radiation lobes, and produces some masking in the directions close to the rotor plane, corresponding to fly-over for an observer on the ground. But a strong overall amplification is observed.

In order to complement the analysis, instantaneous sound-pressure maps in the rotor plane (extraction plane in Fig. 22) are shown in Fig. 24, for the same cases. The free field is characterized by the dominant mode $n = 8$, identified by the number of spiral wavefronts and associated with the aforementioned lobe in Fig. 23, in the outer region. In

[8]The two modes are expected from Tyler & Sofrin's rule. The rotor is made of $B = 10$ blades and the stator of $V = 11$ vanes. At 3BPF, the interaction generates the modes $n = 3 \times 10 - 11s$, s being any relative integer. The lowest values, known to be efficiently radiating, are $n = -3$ (for $s = 3$) and $n = 8$ (for $s = 2$).

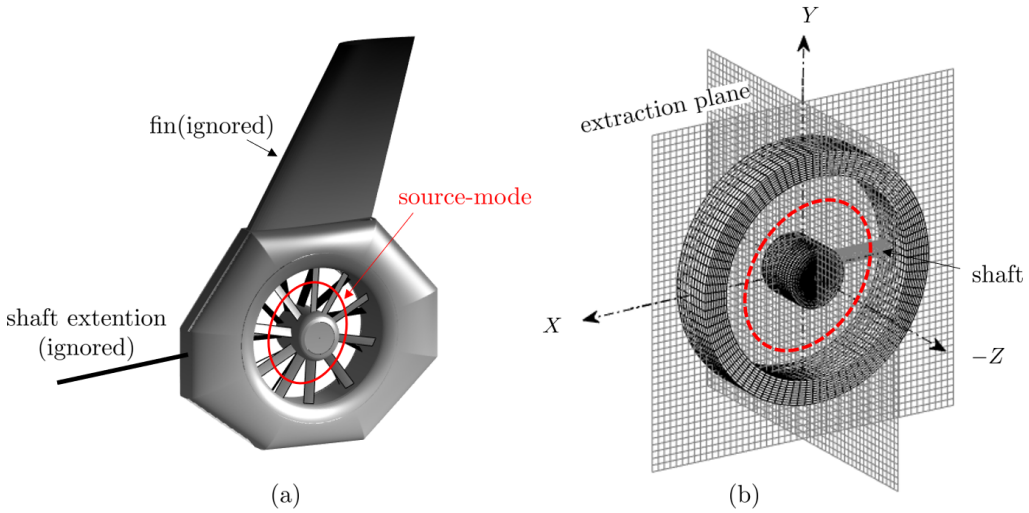


Figure 22: (a): tail-rotor concept (artist view). (b): simplified mesh considered by Roger and Kucukcoskun (2019) for FEM computations shown in Figs. 23 and 24. Source-mode featured in red.

the inner part, the field is dominated by the mode $n = -3$. The rotating phase speeds are indicated by the curved white arrows (Fig. 24-a). Both modes have different wavelengths and spinning phase speeds, at the same considered frequency. Inspection of the maps computed in the installed configuration shows that now, the outer part of the total field is dominated by the mode $n = -3$, the mode $n = 8$ being efficiently masked by the shroud. The mode -3 is less affected because of its larger wavelength. The drastic change of behavior the mode undergoes in the extraction plane is associated with a more general change of the three-dimensional directivity, as obviously recognized in the complementary view of Fig. 23. As expected, including or not the transmission shaft in the mesh does not produce significant changes in the present case.

The assessment of the scattering effect remains of academic nature, in view of the geometrical simplification, accepted for the sake of acceptable computational time. Obviously, the behavior illustrated in Fig. 24 could be observed also on other aerovehicles powered by rotors in short ducts, depending on the parameters. Now it is worth noting that the typical parameters of shrouded helicopter tail rotors correspond to non-compact scattering. Blade numbers range between 8 and 13, BPF are of the order of 600-700 Hz for rotors with evenly spaced blades, for a diameter of 80-90 cm. Ducted rotors of eVTOL aircraft with substantially lower blade numbers somewhat differ from this category. Small-size drones definitely depart from it, entering the class of globally compact objects at the BPF and its first harmonics.

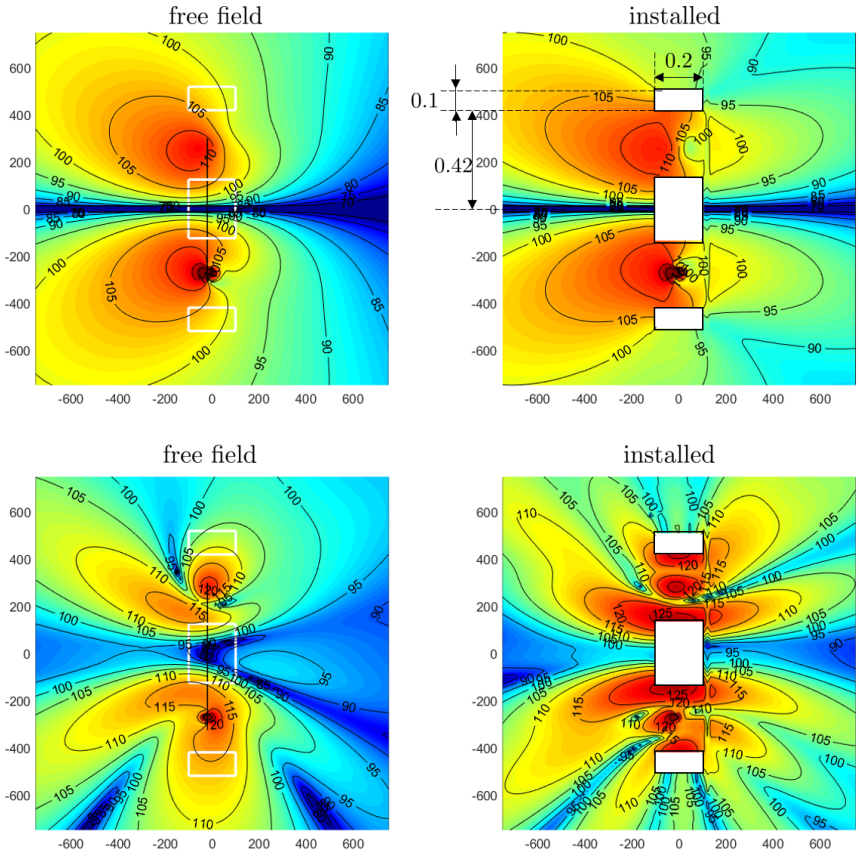


Figure 23: Sound pressure levels predicted by the FEM solver in the vertical meridian plane (Y, Z) at the BPF (487 Hz, top) and at 3BPF (bottom), from Roger and Kucukcoskun (2019). Left: free field, source circle featured by the vertical black segment. Right: total field. Iso-values in dB.

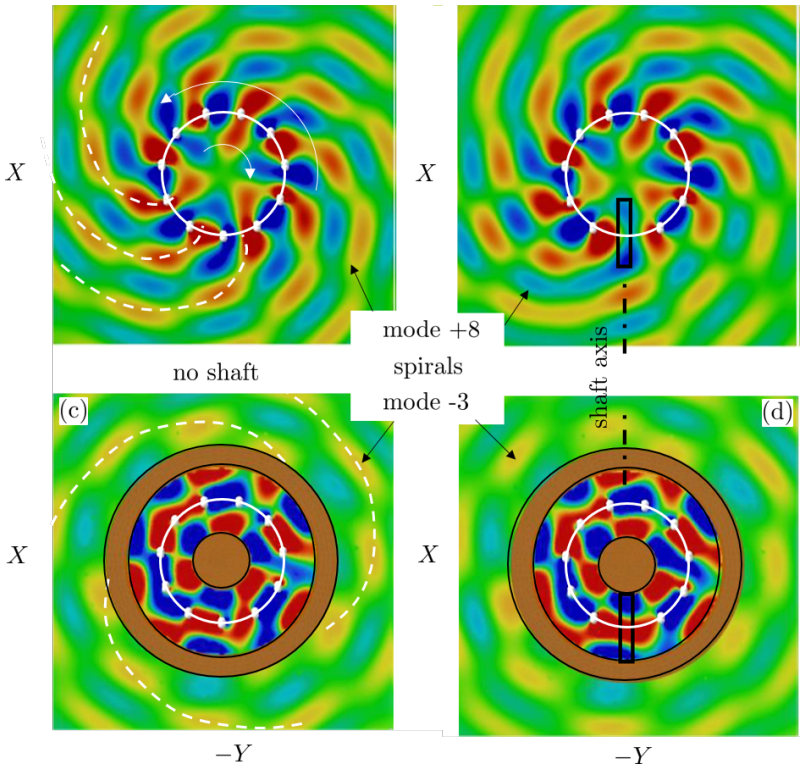


Figure 24: Instantaneous sound-pressure maps computed in the extraction plane of Fig. 22-b, ignoring (a-c) or considering (b-d) the transmission shaft. Free field (a-b) versus total field (c-d). Source circle and spiral wavefronts featured in white.

References

Acevedo Giraldo, D. (2024). *Experimental and analytical investigation of the aerodynamic noise emitted by generic distributed electric propulsion wing-propellers configurations*. PhD thesis, Ecole Centrale de Lyon, France.

Acevedo Giraldo, D., Roger, M., and Jacob, M. (2023). Experimental study of the aerodynamic noise of a pair of pusher-propellers installed over a wing. In *Aviation 2023*, paper 2023-3359, San Diego, CA.

Ahmed, F., Turhan, B., Rezgui, D., and Azarpeyvand, M. (2024). Effect of rotational speed mismatch on a twin propeller system: Aeroacoustics study. In *30th AIAA/CEAS Aeroacoustics Conference*, paper 2024-3420, Rome.

Chaitanya, P., Joseph, P., Prior, S., and Parry, A. (2022). On the optimum separation distance for minimum noise of contra-rotating rotors. *J. Sound & Vib.*, 535:117032.

Colehour, J. and Farquhar, B. (1971). Inlet vortex. *J. of Aircraft*, 8(1):39–43.

Cros, E., Roger, M., and Serre, G. (2023). Low-frequency amplification of propeller tonal noise due to the scattering by a compact rigid cylinder. *J. Sound & Vib.*, 546:17450.

Ffowcs Williams, J. and Hall, L. (1970). Aerodynamic sound generation by turbulent flow in the vicinity of a scattering half plane. *J. Fluid Mech.*, 40(4):657–670.

Gloerfelt, X., Pérot, F., Bailly, C., and Juvé, D. (2005). Flow induced cylinder noise formulated as a diffraction problem for low mach numbers. *J. Sound & Vib.*, 287:129–151.

Gojon, R., Parisot-Dupuis, H., Mellot, B., and Jardin, T. (2023). Aeroacoustic radiation of low reynolds number rotors in interaction with beams. *JASA*, 154:1248–1260.

Greenwood, E., Brentner, K., Rau II, R., and Gan, Z. (2022). Challenges and opportunities for low noise electric aircraft. *Int. J. Aeroacoustics*, 21(5-7):315–381.

Guo, Y., Burley, C., and Thomas, R. (2014). On noise assessment for blended wing body aircraft. In *52nd Aerospace Sciences Meeting*, paper 2014-0365, National Harbor, MD.

Hanson, L., Lim, D., Liu, X., Zhang, B., and Azarpeyvand, M. (2024). A preliminary noise and flow field study of a propeller tilted negatively to a free-stream. In *30th AIAA/CEAS Aeroacoustics Conference*, paper 2024-3385, Rome.

Howe, M. (2003). *Theory of vortex sound*. Cambridge Univ. Press.

Huff, D., Henderson, B., and Cluts, J. (2021). Noise measurements from ground tests of the moog surefly vehicle. In *2021 AIAA AVIATION Forum and Exposition*, doc ID 20210015043, Virtual event.

Jacob, M., Dragna, D., Cahuzac, A., Boudet, J., and Blanc-Benon, P. (2014). Towards hybrid caa with ground effects. *IJA*, 13(3-4):235–259.

Ko, J. and Lee, S. (2023). Quantification of wake interaction effects on multi-rotor configurations in forward flight. *Aero. Sci. & Tech.*, 135:108188.

LeBras, S., Kucukcoskun, K., Acevedo Giraldo, D., and Roger, M. (2024). Aeroacoustic simulations of a pylon-mounted propeller configuration at low reynolds number. In *30th AIAA/CEAS Aeroacoustics Conf.*, paper 2024-3101, Rome.

Leth, S., Samuelsson, F., and Meijer, S. (1998). Propeller noise generation and its reduction on the saab 2000 high-speed turboprop. In *4th AIAA/CEAS Aeroacoustics Conference*, paper 98-2283, Toulouse.

Marulo, F., Solo, A., Aversano, M., Polimeno, U., and Perna, F. (2005). Measurements and predictions of community noise of a pusher-propeller general aviation aircraft. In *11th AIAA/CEAS Aeroacoustics Conf.*, paper 2005-2984, Monterey CA.

Mehrabi, A. and Davari, A. (2020). Outwash flow measurement around the subscale tandem rotor in ground effect. *Eng. Sci. & Tech., Int. J.*, 23:1374–1384.

Misiorowski, M., Gandhi, F., and Oberai, A. (2019). A computational study on rotor interactional effects for a quadcopter in edgewise flight. *AIAA J.*, 57:5309–5319.

Moirou, N., Sanders, D., and Laskaridis, P. (2023). Advancements and prospects of boundary layer ingestion propulsion concepts. *Prog. Aero. Sciences*, 138:100897.

Mukherjee, B. and Brentner, K. (2020). Investigation of propeller-wing interaction noise and the potential contribution to evtol noise. In *VFS Tech. Conf. Aeromech. Design for Transformative Vertical Flight*, San Jose, CA.

Pandey, N., Valdez, J., Beaman, S., and Tinney, C. (2024). Acoustics of side-by-side synchrophased rotors. In *30th AIAA/CEAS Aeroacoustics Conference*, paper 2024-3218, Rome.

Rendon, J., Arroyo Ramo, A., Moreau, S., and Roger, M. (2024). A numerical and analytical approach of the sound-scattering effects in rotor-strut interaction noise of small-size drones. In *30th AIAA/CEAS Aeroacoustics Conf.*, Paper 2024-3047, Rome.

Roger, M. (2022). Some aspects of the tonal noise from installed, subsonic rotors with small blade numbers. In *28th AIAA/CEAS Aeroacoustics Conference*, Award lecture, Southampton.

Roger, M. and Kucukcoskun, K. (2019). Near-and-far field modeling of advanced tail-rotor noise using source-mode expansions. *J. Sound & Vib.*, 453:328–354.

Roger, M. and Moreau, S. (2020). Tonal-noise assessment of quadrotor-type uav using source-mode expansions. *MDPI Acoustics*, 2(3):674–690.

Roger, M., Moreau, S., and Kucukcoskun, K. (2016). On sound scattering by rigid edges and wedges in a flow, with application to high-lift device aeroacoustics. *J. Sound & Vib.*, 362:252–275.

Tinney, C. and Valdez, J. (2024). Hover performance and acoustics of a 35% scale notional evtol rotor. In *30th AIAA/CEAS Aeroacoustics Conference*, paper 2024-3219, Rome.

Vella, E., Gojon, R., Parisot-Dupuis, H., Doué, N., Jardin, N., and Roger, M. (2024). Mutual interaction noise in rotor-beam configuration. In *30th AIAA/CEAS Aeroacoustics Conf.*, paper 2024-3318, Rome.

Zawodny, N. and Boyd, D. (2019). Investigation of rotor-airframe interaction noise associated with small-scale rotary-wing unmanned aircraft systems. *J. Amer. Hel. Soc.*, 65(1).

Zawodny, N., Boyd, D., and Nark, D. (2021). Aerodynamic and acoustic interactions associated with inboard propeller-wing configurations. In *Scitech 2021 Forum*, paper 2021-0714, Virtual event.

Zhang (2017). Measurement of noise from a moving drone using a phased array microphone system. In *APIS Aerosp. Tech.*